



## UvA-DARE (Digital Academic Repository)

### In vivo 808 nm image-guided photodynamic therapy based on an upconversion theranostic nanoplatform

Liu, X.; Que, I.; Kong, X.; Zhang, Y.; Tu, L.; Chang, Y.; Wang, T.T.; Chan, A.; Löwik, C.W.G.M.; Zhang, H.

**DOI**

[10.1039/c5nr03690a](https://doi.org/10.1039/c5nr03690a)

**Publication date**

2015

**Document Version**

Final published version

**Published in**

Nanoscale

**License**

Article 25fa Dutch Copyright Act (<https://www.openaccess.nl/en/policies/open-access-in-dutch-copyright-law-taverne-amendment>)

[Link to publication](#)

**Citation for published version (APA):**

Liu, X., Que, I., Kong, X., Zhang, Y., Tu, L., Chang, Y., Wang, T. T., Chan, A., Löwik, C. W. G. M., & Zhang, H. (2015). *In vivo* 808 nm image-guided photodynamic therapy based on an upconversion theranostic nanoplatform. *Nanoscale*, 7(36), 14914-14923. <https://doi.org/10.1039/c5nr03690a>

**General rights**

It is not permitted to download or to forward/distribute the text or part of it without the consent of the author(s) and/or copyright holder(s), other than for strictly personal, individual use, unless the work is under an open content license (like Creative Commons).

**Disclaimer/Complaints regulations**

If you believe that digital publication of certain material infringes any of your rights or (privacy) interests, please let the Library know, stating your reasons. In case of a legitimate complaint, the Library will make the material inaccessible and/or remove it from the website. Please Ask the Library: <https://uba.uva.nl/en/contact>, or a letter to: Library of the University of Amsterdam, Secretariat, P.O. Box 19185, 1000 GD Amsterdam, The Netherlands. You will be contacted as soon as possible.

UvA-DARE is a service provided by the library of the University of Amsterdam (<https://dare.uva.nl>)



Cite this: *Nanoscale*, 2015, 7, 14914

## *In vivo* 808 nm image-guided photodynamic therapy based on an upconversion theranostic nanoplatfom†

Xiaomin Liu,<sup>a</sup> Ivo Que,<sup>b</sup> Xianggui Kong,<sup>\*a</sup> Youlin Zhang,<sup>a</sup> Langping Tu,<sup>a</sup> Yulei Chang,<sup>a</sup> Tong Tong Wang,<sup>a</sup> Alan Chan,<sup>b,c</sup> Clemens W. G. M. Löwik<sup>b</sup> and Hong Zhang<sup>\*a,d</sup>

A new strategy for efficient *in vivo* image-guided photodynamic therapy (PDT) has been demonstrated utilizing a ligand-exchange constructed upconversion- $C_{60}$  nanophotosensitizer. This theranostic platform is superior to the currently reported nanophotosensitizers in (i) directly bonding photosensitizer  $C_{60}$  to the surface of upconversion nanoparticles (UCNPs) by a smart ligand-exchange strategy, which greatly shortened the energy transfer distance and enhanced the  $^1O_2$  production, resulting in the improvement of the therapeutic effect; (ii) realizing *in vivo* NIR 808 nm image-guided PDT with both excitation (980 nm) and emission (808 nm) light falling in the biological window of tissues, which minimized autofluorescence, reduced light scattering and improved the imaging contrast and depth, and thus guaranteed noninvasive diagnostic accuracy. *In vivo* and *ex vivo* tests demonstrated its favorable bio-distribution, tumor-selectivity and high therapeutic efficacy. Owing to the effective ligand exchange strategy and the excellent intrinsic photophysical properties of  $C_{60}$ ,  $^1O_2$  production yield was improved, suggesting that a low 980 nm irradiation dosage ( $351 \text{ J cm}^{-2}$ ) and a short treatment time (15 min) were sufficient to perform NIR (980 nm) to NIR (808 nm) image-guided PDT. Our work enriches the understanding of UCNP-based PDT nanophotosensitizers and highlights their potential use in future NIR image-guided noninvasive deep cancer therapy.

Received 4th June 2015,  
Accepted 28th July 2015  
DOI: 10.1039/c5nr03690a

www.rsc.org/nanoscale

## 1. Introduction

Photodynamic therapy (PDT) is a non-invasive medical therapeutic technology using photosensitizers (PS) and light irradiation to treat cancers.<sup>1,2</sup> However, current photosensitizers are mostly activated by visible (VIS) light, which restricts PDT to superficial cancers due to light absorption by tissue.<sup>3,4</sup> In recent years, this obstacle has been improved by lanthanide ion ( $\text{Ln}^{3+}$ , such as  $\text{Er}^{3+}$ ,  $\text{Tm}^{3+}$ ,  $\text{Ho}^{3+}$ )-doped upconversion nanoparticles (UCNPs), which are considered as a new generation of multimodal bio-probes, and have attracted great interest for a variety of biological applications.<sup>5–10</sup> The reported luminescence UCNP based nanophotosensitizer (NPS),<sup>11–22</sup> which can be triggered with NIR light ( $\sim 980 \text{ nm}$ ) falling in the biological window of tissues (700–1300 nm), has made PDT capable of treating deeper lesions that could not be realized by visible light. On top of that, this UCNP-based NPS can enhance greatly the quality of imaging because of the significant reduction of the autofluorescence of the background due to the near infrared (NIR) excitation.<sup>23,24</sup>

Up to now, there are three general methods to incorporate PS into UCNP: physical adsorption,<sup>11,13,17</sup> physical encapsulation<sup>12,14–16</sup> and covalent conjugation.<sup>18,19</sup> The physical adsorption method was, at the initial stage, popular, which however inevitably suffered from a low loading capacity and untimely release of PS from UCNPs during blood circulation.<sup>17</sup> Afterwards, physical encapsulation, which could load PS on UCNPs through hydrophobic interaction, was introduced and demonstrated to possess a higher drug loading capacity.<sup>15</sup> However, the high loading capacity of PS did not result in a desired PDT efficiency because of the increased energy transfer distance in such a physical encapsulation.<sup>14</sup> Lately, the developed covalent conjugation of PS to UCNPs has been proved to be able to effectively suppress the leakage of PS from UCNPs.<sup>18</sup> However, the surface of the UCNPs should be firstly functionalized

Up to now, there are three general methods to incorporate PS into UCNP: physical adsorption,<sup>11,13,17</sup> physical encapsulation<sup>12,14–16</sup> and covalent conjugation.<sup>18,19</sup> The physical adsorption method was, at the initial stage, popular, which however inevitably suffered from a low loading capacity and untimely release of PS from UCNPs during blood circulation.<sup>17</sup> Afterwards, physical encapsulation, which could load PS on UCNPs through hydrophobic interaction, was introduced and demonstrated to possess a higher drug loading capacity.<sup>15</sup> However, the high loading capacity of PS did not result in a desired PDT efficiency because of the increased energy transfer distance in such a physical encapsulation.<sup>14</sup> Lately, the developed covalent conjugation of PS to UCNPs has been proved to be able to effectively suppress the leakage of PS from UCNPs.<sup>18</sup> However, the surface of the UCNPs should be firstly functionalized

<sup>a</sup>State Key Laboratory of Luminescence and Applications, Changchun Institute of Optics, Fine Mechanics and Physics, Chinese Academy of Sciences, 130033 Changchun, Jilin, China. E-mail: xgkong14@ciomp.ac.cn

<sup>b</sup>Experimental Molecular Imaging, Department of Radiology, Leiden University Medical Center, 2333 ZA Leiden, The Netherlands

<sup>c</sup>Perucros B.V., Building Zuidhorst, Drienerlolaan 5, 7522 NB Enschede, The Netherlands

<sup>d</sup>Van't Hoff Institute for Molecular Sciences, University of Amsterdam, Science Park 904, 1098 XH Amsterdam, The Netherlands. E-mail: h.zhang@uva.nl

†Electronic supplementary information (ESI) available. See DOI: 10.1039/c5nr03690a

lized with amino or carboxyl groups before covalent conjugation, which still impeded the energy transfer distance.<sup>19</sup> Recently, covalent conjugation and physical absorption of PS to UCNP were combined to maximize the PDT efficacy.<sup>20</sup> In a word, the search for a much more effective conjoint strategy, which could satisfy a high fluorescence resonance energy transfer (FRET) efficiency, has always been a challenge.

In the aforementioned UCNP-based NPSs, upconverted visible light was always applied for imaging, which did not fall in the most favorable area of the biological window (700–1300 nm) and restricted the signal-to-noise ratio. In addition, in all these cases, the NaYF<sub>4</sub>:Yb<sup>3+</sup>,Er<sup>3+</sup> UCNP was the only model for the donor; the limited spectral overlap between Er<sup>3+</sup> and the acceptors restricted the <sup>1</sup>O<sub>2</sub> production yield.<sup>11–22</sup> Typically, most of the currently used photosensitizers are organic dyes, with the drawback of negative side effects, photobleaching and limited <sup>1</sup>O<sub>2</sub> production.<sup>19</sup>

Given this, we have in this work demonstrated a realizable *in vivo* NIR (980 nm) to NIR (808 nm) image-guided PDT utilizing a highly efficient FRET upconversion-C<sub>60</sub> nanoplatform constructed *via* a ligand-exchange approach. Superior to traditional PS, fullerene derivatives possess broad absorption spectra, lack dark toxicity<sup>25</sup> and are “hard” enough to endure relatively high density photoexcitation,<sup>26</sup> and most of all, have nearly 1.0 <sup>1</sup>O<sub>2</sub> quantum yield.<sup>27,28</sup> In so-designed UCNP-C<sub>60</sub>MA NPS, high <sup>1</sup>O<sub>2</sub> production yield was actualized by multiplexed FRET in which multicolor Er<sup>3+</sup> and Tm<sup>3+</sup> separately doping UCNP were the energy donors and C<sub>60</sub>MA the acceptor. Upon 980 nm CW light excitation, upconversion luminescence appeared simultaneously around 360, 407, 450, 475, 540, 650, 696 and 808 nm. All the emissions except 808 nm could transfer energy to C<sub>60</sub>MA to trigger PDT. Meanwhile, 808 nm NIR emission was applied for high contrast NIR luminescence imaging (Scheme 1). It should be emphasized that both excitation and emission were located in the best area of the optical window, which minimized auto-fluorescence and reduced light scattering, and thus guaranteed the non-invasive detection sensitivity. Initially, we followed the covalent

way<sup>19</sup> to construct the UCNP-C<sub>60</sub>MA conjugate. However, the multi-step synthesis and the relatively long distance between UCNP and C<sub>60</sub>MA resulted in a relatively poor <sup>1</sup>O<sub>2</sub> production yield.<sup>34</sup> To improve this situation, a ligand exchange strategy, by which C<sub>60</sub>MA could simply and directly bond to the surface of UCNP, was adopted to greatly shorten the energy transfer distance (see Fig. S2†). Owing to the ligand exchange assembly and excellent intrinsic photophysical properties of C<sub>60</sub>, <sup>1</sup>O<sub>2</sub> production yield was improved, suggesting that a low 980 nm irradiation power density of 0.39 W cm<sup>-2</sup>, which is far below the tolerance for human skin exposure to 980 nm light (0.72 W cm<sup>-2</sup>),<sup>17</sup> and a short treatment time (15 min) were sufficient to perform NIR image-guided PDT. *In vivo* 980 nm NIR-triggered 808 nm NIR imaging and PDT evidenced the high detection sensitivity, favorable bio-distribution, tumor-selectivity and distinct therapeutic efficacy with tumor inhibition ratio up to 78.5%. This study offers an efficient nano-photosensitizer suitable for high quality NIR-to-NIR image-guided therapy of cancer. Furthermore, this ligand-exchange concept can be extended to other systems based on FRET for improving their performances.

## 2. Materials and methods

### 2.1. Materials

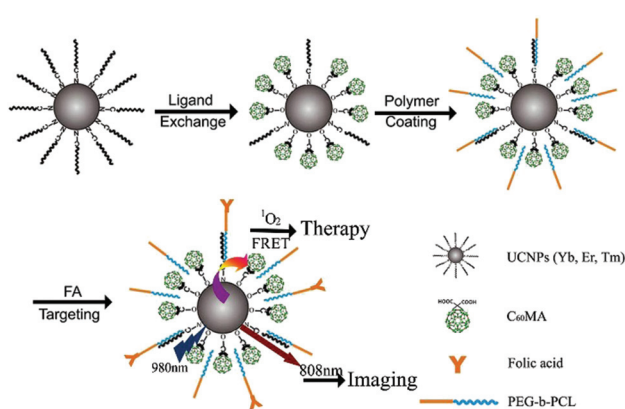
YCl<sub>3</sub>·xH<sub>2</sub>O (99.9%), YbCl<sub>3</sub>·xH<sub>2</sub>O (99.9%), ErCl<sub>3</sub>·xH<sub>2</sub>O (99.9%), TmCl<sub>3</sub>·xH<sub>2</sub>O (99.9%), NaOH (98%), NH<sub>4</sub>F (98%), 1-octadecene (90%), oleylamine (OM), and folic acid were purchased from Sigma-Aldrich. Fluoresceinyl cypridina luciferin analogue (FCLA) was purchased from Tokyo Kasei Kogyo Co., Tokyo, Japan. All chemicals were used as received without further purification. Core, core-shell nanoparticles and monomeric fullerene (C<sub>60</sub>MA) were synthesized according to our previous work.<sup>34</sup>

### 2.2. Synthesis of PEG-*b*-PCL

$\epsilon$ -Caprolactone ( $\epsilon$ -CL) monomer was distilled from calcium hydride and DL-lactide monomer was purified three times by recrystallization in toluene before use. Monomethoxy poly(ethylene glycol) (mPEG-OH,  $M_w = 5000 \text{ g mol}^{-1}$ ) was pre-treated by azeotropic distillation in toluene to remove water. mPEG-OH (2 g) and  $\epsilon$ -CL monomers (2.8 g) were dissolved in anhydrous dichloromethane (100 mL). Hydrochloric acid (2 M in diethyl ether) (0.2 mL) was added as a catalyst and the reaction proceeded at 25 °C under nitrogen for 24 h. mPEG-*b*-PCL block copolymers were precipitated in ice-cold hexane, filtered, and vacuum-dried.

### 2.3. Ligand exchange assembly and surface functionalization

The hydrophobic UCNP solution (~5 mg, purified and dispersed in 2 mL of cyclohexane) was mixed with different amounts of C<sub>60</sub>MA tetrahydrofuran (THF) solution and stirred vigorously over 24 h at 30 °C. UCNP-C<sub>60</sub>MA conjugates were then centrifuged and washed with acetone to remove any unreacted C<sub>60</sub>MA. The obtained nanocomposites were



**Scheme 1** The construction and operating principle of the UCNP-C<sub>60</sub>MA nanophotosensitizer.

redispersed in THF. To surface coat UCNP-C<sub>60</sub>MA with PEG-*b*-PCL molecules, 4 mg PEG-*b*-PCL and 0.5 mg UCNP-C<sub>60</sub>MA nanocomposites were dissolved in 4 mL THF. The above solution was slowly added to 10 mL of deionized water under sonication and stirred for 12 h at room temperature to remove THF. UCNP-C<sub>60</sub>MA conjugates were then centrifuged and washed with water to remove any unreacted PEG-*b*-PCL.

#### 2.4. C<sub>60</sub>MA loading capacity

The concentration of C<sub>60</sub>MA was calculated using the Beer-Lambert law  $A = \epsilon bc$ , where  $A$  represents the absorption value;  $\epsilon$  is the extinction coefficient of C<sub>60</sub>MA which is determined to be 745 l mol<sup>-1</sup> cm<sup>-1</sup> at 514 nm in THF solution;  $b$  equals 1 cm; and  $c$  is the concentration. The absorption value should cover the range from 0.3 to 0.6. UCNPs of 0.5 mg ml<sup>-1</sup> were mixed with various amounts of C<sub>60</sub>MA. After removing free C<sub>60</sub>MA by washing, a certain amount of UCNP-C<sub>60</sub>MA was diluted by THF, and UV-VIS absorption spectra of UCNP-C<sub>60</sub>MA NPs were recorded. UV-VIS absorption spectra of UCNPs were also recorded as the background in the same way. The C<sub>60</sub>MA loading capacity = [amount of C<sub>60</sub>MA in the UCNPs (g)]/[amount of UCNP-C<sub>60</sub>MA (g)] × 100.

#### 2.5. In vitro cell imaging and PDT

0.05 mg folic acid was dissolved in *N,N*-dimethylformamide (DMF) and mixed with 0.5 mg of PEG-*b*-PCL functionalized UCNP-C<sub>60</sub>MA, and stirred for 24 h in the dark. The resulting nanoconjugates were collected by centrifugation, washed with water three times, redispersed in 5 mL of phosphate buffer, and stored in the dark at 4 °C for further application. The concentration of folic acid was also calculated by using the Beer-Lambert law  $A = \epsilon bc$ , where  $\epsilon$  is the extinction coefficient of folic acid which is determined to be 788 l mol<sup>-1</sup> cm<sup>-1</sup> at 360 nm in DMF/water solution. Considering the big overlap between the absorption of C<sub>60</sub>MA and folic acid, we adopted the subtractive absorption process. 1 ml PEG-*b*-PCL functionalized UCNP-C<sub>60</sub>MA (0.6 mg ml<sup>-1</sup>) was mixed with a certain amount of folic acid DMF solution (0.1 mg ml<sup>-1</sup>). Before mixing, the absorption spectrum of the added folic acid solution was determined. After centrifugation, the absorption spectrum of the elute was also recorded. Based on the subtractive absorption value, we can evaluate the amount of folic acid attached to UCNP-C<sub>60</sub>MA NPs. The folic acid loading capacity = [amount of folic acid in the UCNP-C<sub>60</sub>MA (g)]/[amount UCNP-C<sub>60</sub>MA (g)] × 100. It turns out that the loading capacity was 5.1% (w/w). The cell imaging and PDT were carried out according to our previous work<sup>34</sup> with the difference that 0.39 W cm<sup>-2</sup> was set for the 980 nm laser (diode laser, NL-PPS50).

#### 2.6. In vivo imaging

All procedures were approved by the Leiden University animal experimental committee, performed in accordance with the national legislation of the Netherlands and in compliance with the 'Code of Practice Use of Laboratory Animals in Cancer Research' (Inspectie W&V, July 1999). Athymic mice (BALB/c

nu/nu 6 weeks old) were acquired from Charles River (Charles River, L'Arbresle, France) and housed in individually ventilated cages, and food and water were provided *ad libitum*.  $3 \times 10^6$  Hepa1-6 tumor cells were subcutaneously injected into nude mice, and after 2 weeks of tumor growth,  $V = 125 \text{ mm}^3$  and photon intensity =  $10^6 \text{ s}^{-1} \text{ cm}^{-2}$ , 100  $\mu\text{L}$  (3 mg mL<sup>-1</sup>) of UCNP-C<sub>60</sub>MA was administered *iv*. After 2, 24, 48 and 72 hours post injection of UNCP, the mice were imaged by the IVIS Spectrum (Caliper LS, Hopkinton). The interior platform of the animal housing unit of the IVIS Spectrum imager was adapted to hold a clamp which was attached onto a 980 nm laser head. The power supply for the laser was placed outside of the imager but connected by wires inserted through the door entrance of the imager. Organs (heart, liver, spleen, kidney, tumor and bladder) were *ex vivo* measured 72 hours post injection.

#### 2.7. In vivo PDT treatment

Female C57/6J mice (20 g, 6–8 weeks old) used in this study were purchased from the First Bethune Hospital, University of Jilin. All experiments were carried out in compliance with the animal management. The Hepa1-6 tumor model was established by subcutaneously inoculating Hepa1-6 cells ( $3 \times 10^6$ ) into the upper axillary fossa in the mice ( $n = 6$ ). 100  $\mu\text{L}$  saline or UCNP-C<sub>60</sub>MA (3 mg ml<sup>-1</sup>) was intratumorally injected into each Hepa1-6 tumor-bearing mouse. The mice were randomly assigned to four groups treated with different injections, as follows: (1) group 1: subcutaneous injection of the saline (the control group,  $n = 6$ ); (2) group 2: subcutaneous injection of the saline with NIR light irradiation ( $n = 6$ ); (3) group 3: subcutaneous injection of the UCNP-C<sub>60</sub>MA ( $n = 6$ ); (4) group 4: subcutaneous injection of the UCNP-C<sub>60</sub>MA with NIR light irradiation ( $n = 6$ ). The tumors were irradiated with 980 nm laser light (0.39 W cm<sup>-2</sup>) for 15 min. To avoid any tissue damage by heating, the laser treatment was performed at 3 min intervals for every 3 min of light exposure. After treatment, the tumor volume was calculated as length × (width)<sup>2</sup> × 1/2 with a caliper over 2 weeks. The body weight of each mouse was monitored every other day over 2 weeks. Inhibition ratio =  $(V_c - V_t)/V_c \times 100\%$ , where  $V_c$  and  $V_t$  represent the average tumor volume for the control group and treatment group, respectively.

#### 2.8. Statistical analysis

The differences were determined using Student's *t* test where differences were considered significant if  $p < 0.05$ . All data are expressed as the mean ± standard error of the mean.

## 3. Results and discussion

### 3.1. Comparison of C<sub>60</sub> with other photosensitizers

Singlet oxygen production efficiency is the most important factor for PDT. The ideal drug for PDT should have a high quantum yield of <sup>1</sup>O<sub>2</sub>, absorption in the NIR and/or far-IR range, and low toxicity without light irradiation. The most employed photosensitizers for PDT studies are organic dyes,

such as methylene blue (MB), rose bengal (RB), or eosin (EO), which are well known for singlet oxygen generation.<sup>29</sup> Their drawbacks are negative side effects (such as anaphylactic reaction of the skin), photobleaching and limited  $^1\text{O}_2$  production. Lately, fullerene derivatives have been investigated as novel and much more efficient photosensitizers. Such molecules consist of 60 carbon molecules arranged in a characteristic soccer ball shape. The symmetry and the conjugated  $\pi$ -bond system of  $\text{C}_{60}$  result in a number of unique properties, *e.g.* broad absorption and photostability.<sup>30,31</sup> Furthermore, it was evidenced that the singlet oxygen yields of MB, RB, EO and  $\text{C}_{60}$  are 0.1713, 0.0982, 0.0394 and 0.4729, respectively, in benzene–methanol solutions,<sup>29</sup> indicating that the efficiency of singlet oxygen production by  $\text{C}_{60}$  is higher than that of the most frequently used sensitizers in photodynamic studies. For example, it is approximately 12-fold higher than that of EO, and several-fold higher than those of RB and MB. This is mainly because  $\text{C}_{60}$  possesses a high degree of symmetry ( $I_h$ ), and transitions between the ground state and the singlet state are strongly forbidden.<sup>29</sup> This forbiddenness determines that intersystem crossing (ISC) is a dominant process. The triplet state of  $\text{C}_{60}$  is formed in high yield and the triplet lifetime is very long ( $40 \pm 4 \mu\text{s}$ ).<sup>32</sup> Efficient generation of singlet oxygen can thus be obtained by energy transfer from the highly populated  $\text{C}_{60}$  triplet state to the dioxygen ground state.

### 3.2. Ligand-exchange assembly and characterization of the nanophotosensitizer

For energy transfer based PDT, a high energy transfer efficiency is essential for achieving high  $^1\text{O}_2$  production. For this purpose, a ligand exchange strategy was applied to construct the UCNP-based NPS in order to shorten the energy transfer distance. Matching the broad absorption spectrum of fullerene, oleylamine-coated  $\text{NaYF}_4:\text{Yb}^{3+}, \text{Er}^{3+}/\text{NaYF}_4:\text{Yb}^{3+}, \text{Tm}^{3+}$  multicolor UCNP were constructed (see the Experimental section). From the TEM images it could be seen that the UCNP distribute with a diameter of  $34 \pm 5.8 \text{ nm}$  (Fig. 1a, S1†). In oleylamine-coated NPs, the amino groups coordinate to the lanthanide ions ( $\text{Ln}^{3+}$ ) on the surface of the NPs. Considering that the coordination ability of  $\text{Ln}^{3+}-\text{O}$  is stronger than that of  $\text{Ln}^{3+}-\text{N}$ , the carboxyl groups of  $\text{C}_{60}\text{MA}$  could easily replace oleylamine and coordinate to  $\text{Ln}^{3+}$  (Fig. S2a†). Therefore, ligand exchange involved an exchange reaction between the amino group of the ligands in the UCNP and the carboxyl group of  $\text{C}_{60}\text{MA}$ . The ligand exchange process did not affect the size and morphology of UCNP (Fig. 1b). To increase the dispersity of nanocomposites in biology relevant media, poly(ethylene glycol)-*block*-poly(caprolactone) (PEG-*b*-PCL)<sup>33</sup> was used to stabilize the nanocomposites in various biological media (Fig. S3†). Hydrodynamic diameter distributions of the UCNP before and after ligand exchange, and further after polymer coating were measured centered at about 34 nm, 43 nm and 92 nm, respectively, indicating successful surface functionalization (Fig. S4†). FTIR absorption spectra evidenced the success in ligand exchange between UCNP and  $\text{C}_{60}\text{MA}$  (Fig. S5†). The changes in the carbonyl region ( $\nu =$

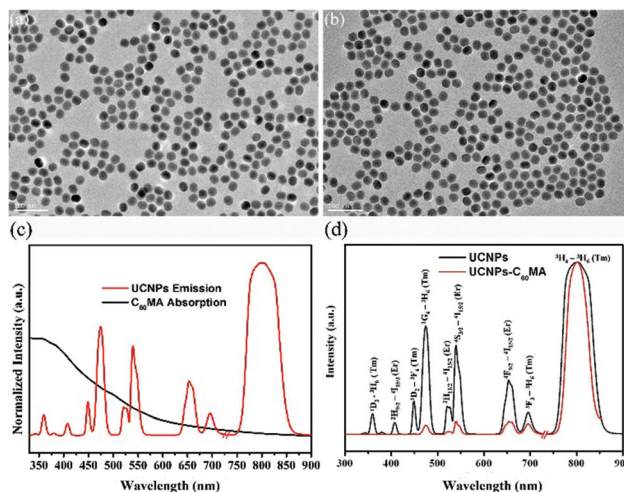


**Fig. 1** (a) TEM images of  $\text{NaYF}_4:\text{Yb}^{3+}, \text{Er}^{3+}/\text{NaYF}_4:\text{Yb}^{3+}, \text{Tm}^{3+}$  core/shell UCNP. (b) TEM images of the ligand exchange assembled UCNP- $\text{C}_{60}\text{MA}$  nanophotosensitizer. (c) Spectral overlap between the emission of the donor UCNP (red) and the absorption of the acceptor  $\text{C}_{60}\text{MA}$  (black). (d) UCL spectra of UCNP and UCNP- $\text{C}_{60}\text{MA}$  nanophotosensitizers (normalized by the intensity at 808 nm; the range from 300 to 730 nm was magnified by a factor of 10).

$1650\text{--}1710 \text{ cm}^{-1}$ ) were taken as indicative of bond formation between the  $\text{C}_{60}\text{MA}$  carboxylic acid group and the inorganic nanoparticles. The binding of  $\text{C}_{60}\text{MA}$  was also confirmed by the fact that dark brown precipitates and nearly colorless supernatants were observed after centrifugation, while no precipitates or color change was noticed in the bare  $\text{C}_{60}\text{MA}$  sample (inset in Fig. S5†).

The payload and stability of the UCNP- $\text{C}_{60}\text{MA}$  NPS were then studied in detail (Fig. S6†). In the  $\text{C}_{60}\text{MA}$  loading process, UCNP were firstly ligand-exchanged with excess  $\text{C}_{60}\text{MA}$ , because ligand-exchange is a dynamic process, and then surface coated with PEG-*b*-PCL. UV-VIS absorption spectra of UCNP- $\text{C}_{60}\text{MA}$  NPS were recorded (see the Experimental section). It was found that the  $\text{C}_{60}\text{MA}$  loading capacity increased with the amount of  $\text{C}_{60}\text{MA}$ , and saturated at 22.5% (w/w) when the amount of  $\text{C}_{60}\text{MA}$  was 0.14 mg (Fig. S6a†), which was approximately twice as high as that of the covalent assembled UCNP- $\text{C}_{60}\text{MA}$  NPS (10.5% w/w) (see Fig. S2b†).<sup>34</sup> The release of  $\text{C}_{60}\text{MA}$  in UCNP- $\text{C}_{60}\text{MA}$  NPS was measured in pH 7.4 PBS, showing a slow release rate with 2.5% of  $\text{C}_{60}\text{MA}$  detached from UCNP after 72 h (Fig. S6b†), which is less than that of the covalently assembled UCNP- $\text{C}_{60}\text{MA}$  NPS (11.2%). The stability was also performed in bovine serum, demonstrating that only 4.8 wt% of  $\text{C}_{60}\text{MA}$  was released from the ligand exchange constructed UCNP- $\text{C}_{60}\text{MA}$  NPS after 72 h (Fig. S6c†). The good stability of the UCNP- $\text{C}_{60}\text{MA}$  NPS facilitated their application in biomedicine.

As mentioned before, the broad absorption spectrum of  $\text{C}_{60}\text{MA}$  overlapped well with the multicolor upconversion luminescence bands (360, 407, 450, 475, 540, 650 and 696 nm) of  $\text{NaYF}_4:\text{Yb}^{3+}, \text{Er}^{3+}/\text{NaYF}_4:\text{Yb}^{3+}, \text{Tm}^{3+}$  (Fig. 1c). Both the steady-

state upconversion luminescence (UCL) spectra and the luminescence decay kinetics evidenced the energy transfer from UCNPs to C<sub>60</sub>MA. The UCL spectrum in Fig. 1d was significantly quenched in the UV-VIS range by C<sub>60</sub>MA. The FRET efficiency, determined from the UCL quench as  $E = (I_0 - I_1)/I_0$ , where  $I_0$  and  $I_1$  are the emission intensities of UCNPs and UCNP-C<sub>60</sub>MA NPS, was 99.7% at 360 nm, 98.3% at 407 nm, 98.7% at 450 nm, 92.7% at 475 nm, 88.2% at 540 nm, 76.2% at 650 nm and 52.3% at 696 nm respectively. The energy transfer efficiency of covalently assembled UCNP-C<sub>60</sub>MA NPS was also measured, as shown in Fig. 2a and Table S1.† After comparison it can be concluded that a ligand-exchange strategy is better than a covalent bonding strategy in reaching a high energy transfer efficiency, and the former is approximately 1.44 times the latter. Such a high energy transfer efficiency was ascribed to the robust ligand-exchange binding between C<sub>60</sub>MA and UCNPs, which improves the stability of the nanoconjugate and shortens the energy transfer distance. On the other hand, the fullerene itself displays advantages over normal fluorescent quenchers and FRET systems in biological applications, with no intrinsic fluorescence emission and the ability to quench a very broad spectrum of phosphors.<sup>31,32</sup>

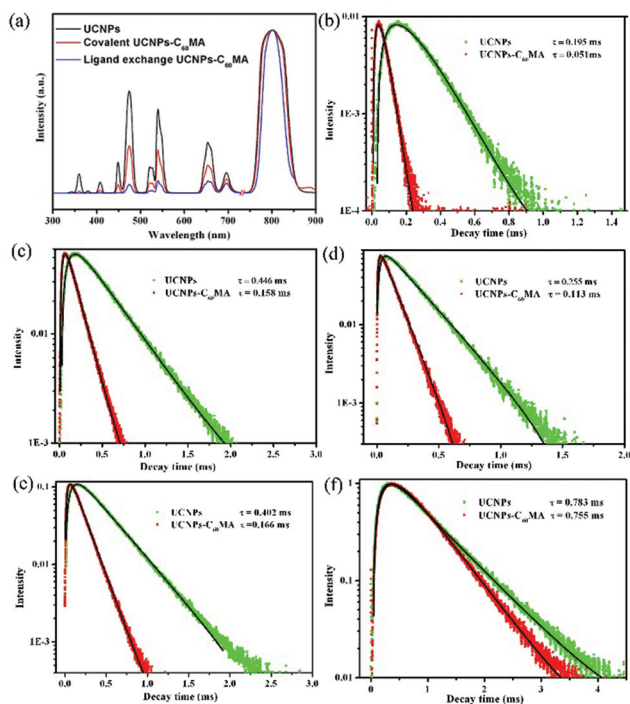


**Fig. 2** (a) UCL spectra of UCNPs (black), covalently conjugated UCNP-C<sub>60</sub>MA (red) and ligand exchange assembled UCNP-C<sub>60</sub>MA (blue) nano-photosensitizers (normalized by the intensity at 808 nm; the range from 300 to 730 nm was magnified by a factor of 10). (b–f) Luminescence decay curves of upconversion emissions monitored (b) at 450 nm, (c) at 475 nm, (d) at 540 nm, (e) at 650 nm, (f) at 808 nm for UCNPs (in green) and ligand exchange assembled UCNP-C<sub>60</sub>MA (red). Best fitting curves are also shown as a black solid line.

The energy transfer process was further studied by the temporal behavior of UCL of both UCNPs and ligand-exchange assembled UCNP-C<sub>60</sub>MA NPS recorded at 450, 475, 540, 650 and 808 nm (Fig. 2b–f). In all cases, the decay curves could be well fitted with a bi-exponential function. In the presence of C<sub>60</sub>MA, however, the average decay time decreases from 195 μs to 51 μs for 450 nm, from 446 μs to 158 μs for 475 nm, from 255 μs to 113 μs for 540 nm and from 402 μs to 166 μs for 650 nm, respectively. The significant shortening of the UCL kinetics is consistent with the efficient energy transfer obtained from the steady-state UCL quenching. The average decay time at 808 nm shows hardly any change because of the poor absorption of C<sub>60</sub>MA in the NIR region. The FRET efficiencies, calculated based on the change of temporal behavior (Table S2†), show efficiencies of 72.8% at 450 nm, 63.1% at 475 nm, 56.3% at 540 nm and 50.8% at 650 nm, which are a little less compared with the values determined from steady-state UCL spectra (98.7% at 450 nm, 92.7% at 475 nm, 88.2% at 540 nm, 76.2% at 650 nm). This is mainly because with the increase of PS loading amounts, although most of them are closely attached to the surface of the UCNPs, the re-absorption process becomes inevitable due to the strong quenching ability of C<sub>60</sub>MA.<sup>35</sup> Both re-absorption and FRET contributed to the luminescence quench. However, the re-absorption does not affect the temporal behavior of UCNPs, and the shortening of the UCL lifetimes reflects specifically the FRET process. The efficient multiplexed FRET from UCNPs to C<sub>60</sub>MA ensured high <sup>1</sup>O<sub>2</sub> generation.

Another motivation for designing the UCNP-C<sub>60</sub>MA NPS was the high <sup>1</sup>O<sub>2</sub> production yield of C<sub>60</sub> derivatives, which has been proved to be even better than that of traditional photosensitizers. In order to assess the <sup>1</sup>O<sub>2</sub> generation of UCNP-C<sub>60</sub>MA NPS, fluoresceinyl cypridina luciferin analogue (FCLA), which can be oxidized by <sup>1</sup>O<sub>2</sub> leading to an increase of its fluorescence around 524 nm, was used as a <sup>1</sup>O<sub>2</sub> indicator.<sup>36</sup> Fig. S7† shows the fluorescence spectra of FCLA for ligand exchange and covalently conjugated UCNP-C<sub>60</sub>MA NPS, respectively. The corresponding fluorescence intensity changes at 524 nm are depicted in Fig. 3a. The slopes of the curves represent the efficiency of singlet oxygen generation; the higher slope of the ligand exchange assembled UCNP-C<sub>60</sub>MA NPS indicates distinctly its higher <sup>1</sup>O<sub>2</sub> yield. It should be noted that the ligand exchange assembled UCNP-C<sub>60</sub>MA NPS results in twice the amount of C<sub>60</sub>MA loaded compared to the covalent route. However, the generation of reactive oxygen seems to be less than this factor. This is mainly because various factors may affect the <sup>1</sup>O<sub>2</sub> production, including, among others, the energy transferred from the nanoparticle to the C<sub>60</sub>MA, the loading capacity of the photosensitizers, the oxygen concentration of the area, and the triplet state lifetime of the photosensitizers. The location of the photosensitizers is also critical since the energy transfer depends strongly on the distance between the energy donor and acceptor. Therefore, the generation of reactive oxygen is not a simple linear process with regard to the loading capacity of the photosensitizer.

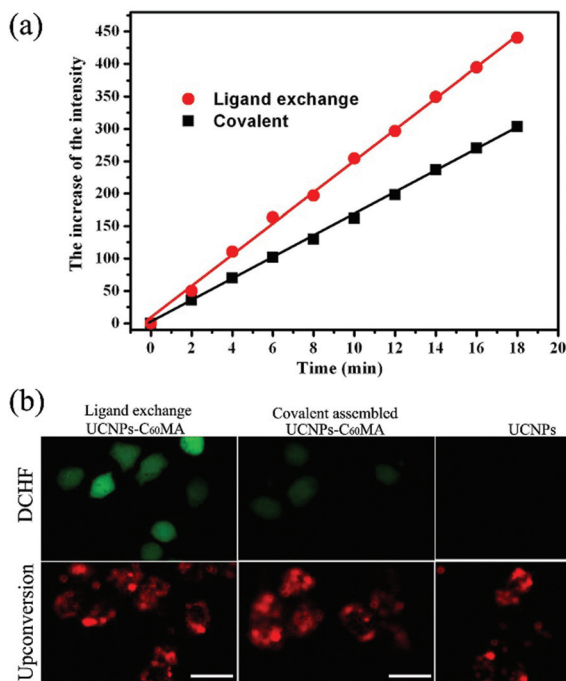


**Fig. 3** (a) The increase in luminescence intensity of FCLA at 524 nm as a function of the exposure time under 980 nm irradiation. (b) Detection of intracellular reactive oxygen production by DCFH-DA staining in HeLa cells incubated with ligand exchange assembled UCNP-C<sub>60</sub>MA NPS (left), covalently conjugated UCNP-C<sub>60</sub>MA (middle) and void UCNPs (right). Scale bar, 20  $\mu\text{m}$ .

We also examined the production of <sup>1</sup>O<sub>2</sub> from the NPS in live cells using 2,7-dichlorofluorescein-diacetate (DCFH-DA) as a fluorogenic marker for <sup>1</sup>O<sub>2</sub>. DCFH-DA distributes in live cells and, in the presence of <sup>1</sup>O<sub>2</sub>, was oxidized to emit bright green fluorescence. We irradiated HeLa cells labeled with ligand exchange and covalently conjugated UCNP-C<sub>60</sub>MA NPS under the same 980 nm light dosage (0.39 W cm<sup>-2</sup> for 5 min), respectively. The resulting oxidatively stressed cells showed green fluorescence as can be seen in Fig. 3b, indicating an increase in <sup>1</sup>O<sub>2</sub>, whereas control cells treated only with UCNPs showed negligible fluorescence. Notably, the green fluorescence of the cells treated with ligand exchange assembled NPS was more intense than that of the covalently conjugated ones, which further confirmed the strong <sup>1</sup>O<sub>2</sub> generation and the superiority of a ligand exchange strategy.

### 3.3. *In vitro* cancer cell uptake and photodynamic killing

With the <sup>1</sup>O<sub>2</sub> generation of the UCNP-C<sub>60</sub>MA NPS having been demonstrated, we have studied the targeting cellular uptake of UCNP-C<sub>60</sub>MA NPS using HeLa cells. To achieve the tumor targeting property, folic acid (FA) was attached to PEG-*b*-PCL functionalized UCNP-C<sub>60</sub>MA NPS.<sup>37,38</sup> The loading capacity of folic acid reached 5.1% (w/w) (see the Experimental section). Fig. S8† shows the target staining of the UCNP-C<sub>60</sub>MA/FA NPS in HeLa cells (FR-positive)<sup>15</sup> and the control result in human alveolar adenocarcinoma (A549) cells (FR-negative).<sup>22</sup> The UCL

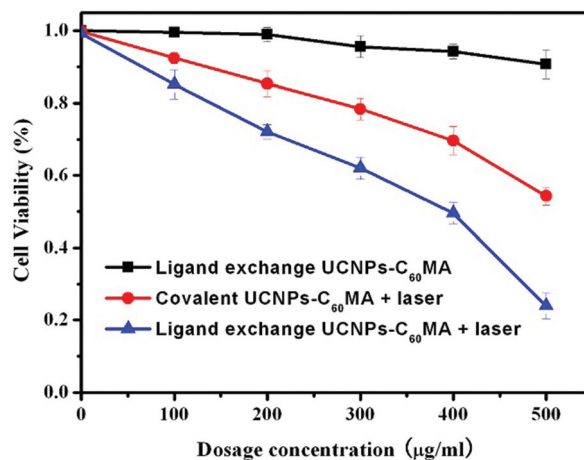


**Fig. 4** The photodynamic capabilities of covalently conjugated UCNP-C<sub>60</sub>MA (red; 980 light dosage: 1.37 W cm<sup>-2</sup> for 10 min) and ligand exchange assembled UCNP-C<sub>60</sub>MA NPS (blue; 980 light dosage: 0.39 W cm<sup>-2</sup> for 10 min).

was collected at 808 nm – a wavelength that lies in the minimal absorption range and enables high-contrast optical imaging and high treatment depth.<sup>39</sup> The nanocomposites were mainly located inside the cells (Fig. S8,† left), illustrating the specific targeting of the NPS. For A549 cells, which are poor at expressing the folate receptor, few UCNP-C<sub>60</sub>MA/FA NPS were stained (Fig. S8,† right).

The NIR light triggered photodynamic therapy of cancer cells by UCNP-C<sub>60</sub>MA/FA NPS was firstly studied *in vitro*. HeLa cells were incubated with NPS at different concentrations. The cell viability as determined from the MTT assay is shown in Fig. 4. The dark toxicity became non-negligible only when the concentration was higher than 500  $\mu\text{g mL}^{-1}$  (100  $\mu\text{L}$ ), at which point the cell viability went down to nearly 90%. When HeLa cells were exposed to 980 nm NIR light at a relatively low density of 0.39 W cm<sup>-2</sup> for 10 min, the cells' decline could be observed. The decline was getting faster with the increase of the NPS concentration. It was also evidenced from Fig. S9† that most of the cells treated with 100  $\mu\text{g mL}^{-1}$  (100  $\mu\text{L}$ ) NPS kept their healthy spindle morphologies upon light exposure. When the dosage was increased to 300  $\mu\text{g mL}^{-1}$  (100  $\mu\text{L}$ ), the majority of them were dead. On increasing further the dosage to 500  $\mu\text{g mL}^{-1}$  (100  $\mu\text{L}$ ), almost all of the cells shrank and lost their normal morphology. Photodynamic therapy using the covalently conjugated UCNP-C<sub>60</sub>MA model was also tested under similar conditions for comparison, which was obviously less efficient, emphasizing the superior cancer cell killing ability of the designed ligand exchange UCNP-C<sub>60</sub>MA photosensitizing nanoplatform. Besides the human HeLa cell, the mouse Hepa1-6 cell line was chosen for *in vitro* test (Fig. S10†), also demonstrating an efficient PDT effect.

### 3.4. *In vivo* tumor-targeting and therapeutic efficacy

The *in vivo* bio-distribution and tumor targeting ability of the UCNP-C<sub>60</sub>MA/FA NPS were tracked in mice bearing Hepa1-6

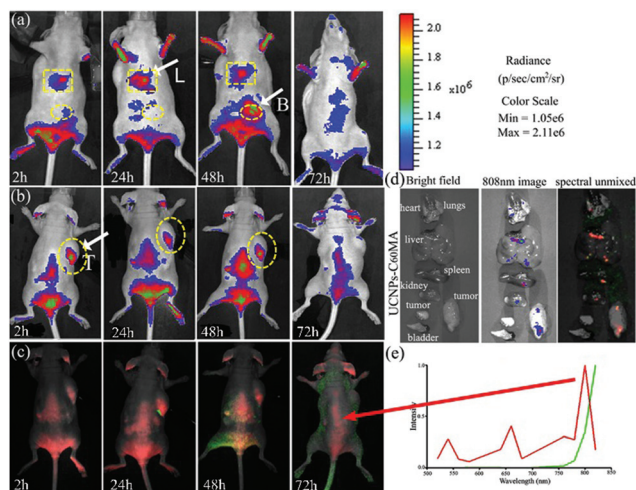


**Fig. 5** *In vivo* tumor-targeting and biodistribution of the UCNP-C<sub>60</sub>MA/FA nanophotosensitizer. Fluorescence images of nude mice bearing Hepa1-6 tumor. Images were taken at different time points after iv injection of the UCNP-C<sub>60</sub>MA nanophotosensitizer: (a) ventral images; (b) dorsal images and (c) dorsal spectral unmixed images. Arrows mark the location of the tumor (T), liver (L), and bladder (B). (d) Fluorescence images of isolated organs separated from mice of different groups at 72 h post-injection. (e) PL spectra corresponding to the spectrally unmixed components of the multispectral image; the red color indicates 808 nm emission from UCNPs and the green color is autofluorescence.

tumors (FR-positive),<sup>40</sup> which were administrated NPS and imaged at different times (Fig. 5). Two hours after *in vivo* tail vein injection, the 808 nm luminescence emitted from NPS was distinctly visualized in the superficial vasculature of the mouse. Subsequently, as blood circulated, the NPSs were seen to gradually distribute and deposit inside different organs. Significant tumor uptake was clearly visible in mice treated with NPS after 2 h post-injection (pi). By 24 h pi, the maximal tumor luminescence was attained and it persisted for more than 48 h pi. The NPS exhibited a prominent distribution in tumor, liver and bladder after 48 h pi. By 72 h pi, the NPSs were cleared from the circulation and the luminescence signals in the liver decreased, but were still visible. As indicated by the luminescence signal, NPS remained visible in the circulation even after 72 h pi (Fig. 5a and b). The spectral unmixed, high contrast images (Fig. 5c) clearly demonstrate the feasibility of imaging and spectrally distinguishing the characteristic emission of the NPS (shown in red). A scan in the range of 700–820 nm showed an intense NIR luminescence peaking at ~800 nm, strongly evidenced by 808 nm NIR imaging (Fig. 5e). The high contrast between the background and the luminescence signal from NPS came from NIR-to-NIR upconversion luminescence imaging.

To further support the tumor selective targeting of the designed nanophotosensitizer, the results of mice bearing tumors are provided in Fig. S11† which were administered UCNP-C<sub>60</sub>MA/FA or UCNP-C<sub>60</sub>MA and imaged at different time points. Tumor uptake in mice treated with UCNP-C<sub>60</sub>MA

became visible only at 24 h post-injection as a result of enhanced permeation and retention (EPR effect) in the tumor accumulation of the NPs, whereas UCNP-C<sub>60</sub>MA/FA were already accumulated in the tumor area at 2 h post-injection. To confirm the *in vivo* imaging results, *ex vivo* organ optical imaging has been performed. Fig. 5d shows *ex vivo* optical images of resected organs at 72 h pi. It is obvious that relatively intensive luminescence of UCNP-C<sub>60</sub>MA/FA NPS remained mainly in the tumor, liver and kidney. However, the respective organs of uninjected mice showed no comparable luminescence (Fig. S12†). The results demonstrated that the major sites of luminescence seen by *ex vivo* optical imaging were in line with those seen in noninvasive imaging, supporting the high tumor selectivity and indicating also that the bio-distribution of the designed NPS inside organs could be sensed and imaged *in vivo*.

With the tumor uptake of the nanoplatform having been demonstrated, *in vivo* PDT treatment by UCNP-C<sub>60</sub>MA NPS was explored in Hepa1-6 tumor-bearing C57/6J mice, which have an immune system and can be raised in a natural environment. Moreover, such kinds of mice are similar to human tumor patients in pathological change. Therefore they are appropriate for PDT studies. The Hepa1-6 tumor model was established by subcutaneously inoculating Hepa1-6 cells ( $3 \times 10^6$ ) into the upper axillary fossa in the mice ( $n = 6$ ). The tumors were irradiated with 980 nm laser light at  $0.39 \text{ W cm}^{-2}$  for 15 min, namely the 980 nm irradiation dosage was  $351 \text{ J cm}^{-2}$ . It is worth noting that the NIR laser power used here ( $0.39 \text{ W cm}^{-2}$ ) is far below the conservative limits set for human skin exposure to 980 nm light ( $0.72 \text{ W cm}^{-2}$ ).<sup>17</sup> We found no skin burn scars caused by the generation of excessive local heating ascribed to the NIR laser irradiation in any of the mice (Fig. 6a). After treatment, the tumors were isolated from the different groups of mice and weighed. As can be seen from Fig. 6a and b, the mice treated with saline, just 980 nm light irradiation or NPS without light irradiation did not show any

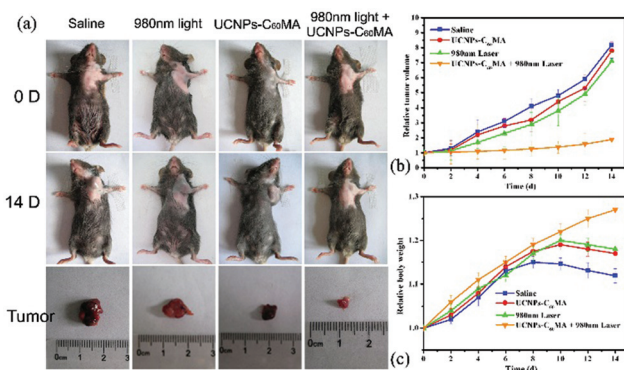


**Fig. 6** (a) Representative photos of mice and tumor before and after various treatments indicated. (b) Tumor growth of mice in different treatment groups within 14 days. (c) Changes of body weight of mice in different groups during PDT.  $n = 6$  per group;  $p < 0.05$ ; error bars represent standard errors of the mean.

therapeutic effect, while the mice that received injection of the NPS with 980 nm NIR light irradiation show a very high tumor inhibition ratio (78.5%). Body weight changes can also reflect the health condition of the treated mice. As shown in Fig. 6c, the body weight of mice of the control group began to decrease from day 8 post-treatment, which indicates that the living quality of the mice was affected by the tumor burden. For the PDT treated group, their body weight gradually increased during 14 days, demonstrating that PDT treatment based on UCNP-C<sub>60</sub>MA NPS can effectively improve the survival quality of mice and prolong their lifetime. It should be emphasized that the lowest irradiation power used for the PDT based on UCNP studies to date was 360 J cm<sup>-2</sup> with the nanophotosensitizer dosage of 50 mg kg<sup>-1</sup>.<sup>42</sup> However, the situation has greatly improved in our study in that under the irradiation power of 351 J cm<sup>-2</sup> and a drug dosage of only 17 mg kg<sup>-1</sup>, the tumor inhibition ratio can reach up to 78.5% when using the designed nanophotosensitizer, evidencing that the efficient energy transfer benefited from the ligand-exchange construction.

We further extended the study to examine the targeted PDT efficacy of UCNP-C<sub>60</sub>MA/FA NPS. The experimental details were the same as what we did in intratumoral injection with the exception that UCNP-C<sub>60</sub>MA/FA or UCNP-C<sub>60</sub>MA nanophotosensitizers were intravenously injected into the mice bearing Hepa1-6 tumors. It should be noted that the light spot we used could only cover the tumor area. By selectively irradiating only the disease site, little or no damage is incurred by the surrounding healthy tissues. Therefore, for *in vivo* targeted PDT, we need to gain information from *in vivo* imaging such as how long the nanophotosensitizer could accumulate and remain in the tumor after iv injection. As indicated in Fig. 5b, the concentration of the nanophotosensitizer in the tumor can be reflected by the intensity of the NIR luminescence signal. Significant tumor uptake was clearly visible in mice treated with the nanophotosensitizer after 2 h post-injection (pi) and persisted for more than 48 h pi. Under the guidance of this information, after 2 h pi, the tumors were irradiated with 980 nm laser light at 0.39 W cm<sup>-2</sup> for 15 min every day. In addition, the nanophotosensitizers have to be intravenously injected every 3 days to guarantee that the nanophotosensitizers exist in the tumor. We found no such significant anti-tumor effect in mice treated with saline or only under 980 nm light irradiation. The mice that received intravenous injection of UCNP-C<sub>60</sub>MA/FA NPS showed a relatively higher tumor inhibition ratio (66.3%) than that of the control mice treated with folic acid unmodified UCNP-C<sub>60</sub>MA NPS (33.5%), indicating that active targeting by modifying the surface of the NPS with cancer-specific targeting agents has an important role in improving the therapeutic efficacy for a desirable PDT outcome (Fig. 7a). The histological analysis of the tumor, heart, liver, spleen, lung, and kidney was carried out in different treatment groups after 14 days of post-treatment. It can be clearly observed in Fig. 7b that the morphology, size and staining of the tumor cells in the saline group are at variance, and mitotic figures are seen in most nuclei. It is a

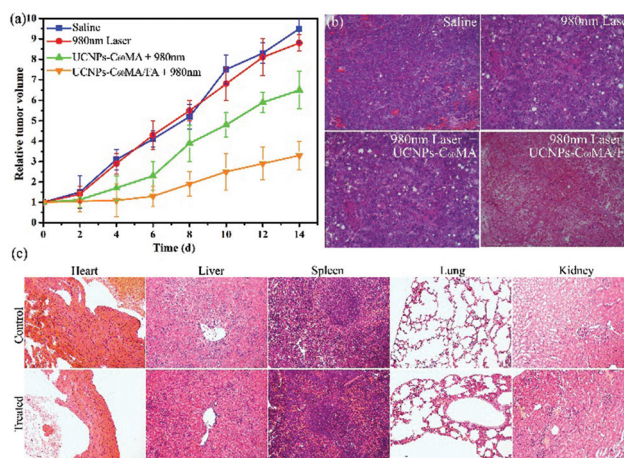


Fig. 7 (a) Tumor growth of mice in different treatment groups within 14 days.  $n = 6$  per group;  $p < 0.05$ ; error bars represent standard errors of the mean. H&E stained images of (b) the tumor, (c) heart, liver, spleen, lung, and kidney collected from different groups.

similar situation for the 980 nm laser group. However, markedly increased apoptotic and necrotic tumor cells were observed in targeted PDT treatment groups. Histological analysis shown in Fig. 7c reveals no pathological changes in the heart, lung, kidney, liver or spleen. Hepatocytes in the liver samples were found to be normal. No pulmonary fibrosis was detected in the lung samples. The glomerulus structure in the kidney section was observed clearly. Necrosis was not found in any of the histological samples analyzed. These results clearly demonstrate the targeted PDT efficacy of the as-designed UCNP-C<sub>60</sub>MA/FA NPS. There are three main mechanisms involved in this PDT mediated tumour destruction.<sup>41</sup> In the first case, the singlet oxygen that is generated by PDT can kill tumor cells directly. PDT also damages the tumor-associated vasculature, leading to tumor infarction. Finally, PDT can activate an immune response against tumor cells. Notably, the tumor inhibition ratio of intravenous injection (66.3%) was smaller than that of intratumoral injection (78.5%), because intravenous injection might face physiological barriers, such as spatially and temporally heterogeneous blood flow, and high vascular permeability. Even in intratumoral injection, the tumors were not completely regressed as a result of injection of UCNP-C<sub>60</sub>MA NPS and irradiation, as is expected in an ideal scenario of cancer therapy. Further optimization of the experimental conditions is still required to exploit the full potential of these NPSs as a PDT drug to be used in the clinic. These may include optimization of UCNP synthesis for even brighter UCL emission, and further improvement of the <sup>1</sup>O<sub>2</sub> generation or the dose of NPS injected.

## 4. Conclusions

In this work, we have proposed a feasible *in vivo* 808 nm image-guided PDT based on an effective upconversion-C<sub>60</sub>

nanoplatfom constructed *via* a ligand-exchange strategy, which could greatly improve the FRET efficiency between the donor and the acceptor by shortening the energy transfer distance. Owing to the optimized FRET efficiency and the monomeric fullerene (C<sub>60</sub>MA) PS molecules which exhibit nearly 100% <sup>1</sup>O<sub>2</sub> yield, high <sup>1</sup>O<sub>2</sub> production yield was achieved, suggesting that NIR illumination powers as low as 351 J cm<sup>-2</sup> were sufficient to perform simultaneous imaging and PDT. Based on the results of NIR imaging, the designed nanoplatfom was demonstrated to exhibit a high noninvasive detection sensitivity, a favorable bio-distribution and an enhanced tumor-selectivity. Tests performed on *in vivo* PDT evidenced its remarkable therapeutic efficacy. These results indicate that the upconversion-C<sub>60</sub> NPS is a promising PDT agent for NIR-to-NIR simultaneous diagnosis and therapy.

## Acknowledgements

This work was financially supported by NSF of China (11174277, 11374297, 11474278, 61275202, and 21304084), Joint research program between CAS of China and KNAW of the Netherlands, the IOP program of The Netherlands, and the John van Geuns Foundation.

## Notes and references

- A. P. Castano, P. Mroz and M. R. Hamblin, *Nat. Rev. Cancer*, 2006, **6**, 535.
- L. R. Braathen, R. M. Szeimies, N. B. Seguin, B. Bissonnette, P. Foley, D. Pariser, R. Roelandts, A. M. Wennberg and C. A. Morton, *J. Am. Acad. Dermatol.*, 2007, **56**, 125.
- P. Rai, S. Mallidi, X. Zheng, R. Rahmzadeh, Y. Mir, S. Elrington, A. Khurshid and T. Hasan, *Adv. Drug Delivery Rev.*, 2010, **62**, 1094.
- J. P. Celli, B. Q. Spring, I. Rizvi, C. L. Evans, K. S. Samkoe, S. Verma, B. V. Pogue and T. Hasan, *Chem. Rev.*, 2010, **12**, 2795.
- N. J. J. Johnson, A. Korinek, C. H. Dong and F. C. J. M. Van Veggel, *J. Am. Chem. Soc.*, 2012, **134**, 11068.
- F. Zhang, Y. F. Shi, G. B. Braun, Y. C. Zhang, X. H. Sun, N. O. Reich, D. Y. Zhao and G. D. Stucky, *J. Am. Chem. Soc.*, 2010, **132**, 2850–2851.
- H. S. Mader, S. P. Kele, M. Saleh and O. S. Wolfbeis, *Curr. Opin. Chem. Biol.*, 2010, **14**, 582.
- F. Wang and X. G. Liu, *Chem. Soc. Rev.*, 2009, **4**, 976.
- M. Haase and H. Schäfer, *Angew. Chem., Int. Ed.*, 2011, **50**, 5808.
- Y. Liu, K. Ai, J. Liu, Q. Yuan, Y. He and L. H. Lu, *Angew. Chem., Int. Ed.*, 2011, **51**, 1437.
- P. Zhang, W. Steelant, M. Kumar and M. Scholfield, *J. Am. Chem. Soc.*, 2007, **129**, 4526.
- K. C. Dev and Y. Zhang, *Nanomedicine*, 2008, **3**, 73.
- H. Qian, H. Guo, P. Ho, R. Mahendran and Y. Zhang, *Small*, 2009, **5**, 2285–2290.
- J. N. Shan, S. J. Budijono, G. Hu, N. Yao, Y. Kang, Y. Ju and P. K. Prud'homme, *Adv. Funct. Mater.*, 2011, **21**, 2488.
- C. Wang, H. Tao, L. Cheng and Z. Liu, *Biomaterials*, 2011, **32**, 6145.
- M. E. Lim, Y. L. Lee, Y. Zhang and J. J. H. Chu, *Biomaterials*, 2012, **33**, 1912.
- N. M. Idris, M. K. Gnanasammandhanl, J. Zhang, P. C. Ho, R. Mahendran and Y. Zhang, *Nat. Med.*, 2012, **18**, 1580.
- X. F. Qiao, J. C. Zhou, J. W. Xiao, Y. F. Wang, L. D. Sun and C. H. Yan, *Nanoscale*, 2012, **4**, 4611.
- K. Liu, X. M. Liu, Q. H. Zeng, Y. L. Zhang, L. P. Tu, T. Liu, X. G. Kong, Y. Wang, F. Cao, S. A. Lambrechts and H. Zhang, *ACS Nano*, 2012, **6**, 4054.
- Y. I. Park, H. M. Kim, J. H. Kim, K. C. Moon, B. Yoo, K. T. Lee, N. Lee, Y. Choi, W. Park and D. Ling, *Adv. Mater.*, 2012, **24**, 5755.
- S. Cui, H. Chen, H. Zhu, J. Tian, Z. Qian, S. Achilefu and Y. Q. Gu, *J. Mater. Chem.*, 2012, **22**, 4861.
- S. S. Cui, D. Y. Yin, Y. Q. Chen, Y. F. Di, H. Y. Chen, Y. X. Ma, S. Achilefu and Y. Q. Gu, *ACS Nano*, 2013, **7**, 676.
- H. Guo, H. Qian, N. M. Idris and Y. Zhang, *Nanomedicine*, 2009, **6**, 486.
- F. Wang, D. Banerjee, Y. S. Liu, X. Y. Chen and X. G. Liu, *Analyst*, 2010, **135**, 1839.
- D. M. Guldi and M. Prato, *Acc. Chem. Res.*, 2000, **33**, 695.
- S. Fukuzumi, T. Suenobu, M. Patz, T. Hirasaka, S. Ito and M. Fujitsuka, *J. Am. Chem. Soc.*, 1998, **120**, 8060.
- H. Fueno, Y. Takenaka and K. Tanaka, *Opt. Spectrosc.*, 2011, **111**, 248.
- J. W. Arbogast and C. S. Foote, *J. Am. Chem. Soc.*, 1991, **113**, 8886.
- T. Nagano, K. Arakane, A. Ryu, T. Masuanga, K. Shinmoto, S. Mashiko and M. Hirobe, *Chem. Pharm. Bull.*, 1994, **42**, 2291.
- J. W. Arbogast, A. P. Darmany, C. S. Foote, Y. Rubin, F. N. Diederich, M. M. Alvarez, S. J. Anz and R. L. Whetten, *J. Phys. Chem.*, 1991, **95**, 11.
- K. D. Pickering and R. Wiesner, *Environ. Sci. Technol.*, 2005, **39**, 1359.
- T. Da Ros and M. Prato, *Chem. Commun.*, 1999, 663.
- B. Ungun, R. K. Prud'homme, S. J. Budijono, J. N. Shan, S. F. Lim, Y. G. Ju and R. Austin, *Opt. Express*, 2009, **17**, 80.
- X. M. Liu, M. Zheng, X. K. Kong, Y. L. Zhang, Q. H. Zeng, Z. C. Sun, W. J. Buma and H. Zhang, *Chem. Commun.*, 2013, **49**, 3224.
- S. M. Saleh, R. Ali, T. Hirsch and O. S. Wolfbeis, *J. Nanopart. Res.*, 2011, **13**, 4603.
- A. G. Zhou, Y. C. Wei, B. Y. Wu, Q. Chen and D. Xing, *Mol. Pharm.*, 2012, **9**, 1580.
- S. Chen, X. Z. Zhang, S. X. Cheng, R. X. Zhou and Z. W. Gu, *Biomacromolecules*, 2008, **9**, 2578.
- L. M. Yao, J. Zhou, J. L. Liu, W. Feng and F. Y. Li, *Adv. Funct. Mater.*, 2012, **22**, 2667.

- 39 M. Nyk, R. Kumar, T. Y. Ohulchansky, E. J. Bergey and P. N. Prasad, *Nano Lett.*, 2008, **8**, 3834.
- 40 A. M. Nour, D. Ringot, J. L. Gueant and A. Chango, *Carcinogenesis*, 2007, **28**, 2291.
- 41 D. E. Dolmans, D. Fukumura and R. K. Jain, *Nat. Rev. Cancer*, 2003, **3**, 380.
- 42 N. M. Idris, M. K. G. Jayakumar, A. Bansal and Y. Zhang, *Chem. Sov. Rev.*, 2015, **44**, 1449.